Article

Observing dynamical phases of BCS superconductors in a cavity QED simulator

https://doi.org/10.1038/s41586-023-06911-x

Received: 21 June 2023

Accepted: 29 November 2023

Published online: 24 January 2024

Check for updates

Dylan J. Young[1,6], Anjun Chu[1,2,6], Eric Yilun Song[1], Diego Barberena[1,2], David Wellnitz[1,2], Zhijing Niu[1], Vera M. Schäfer[1,3], Robert J. Lewis-Swan[4,5], Ana Maria Rey[1,2]✉ & James K. Thompson[1]✉

In conventional Bardeen–Cooper–Schrieffer superconductors[1], electrons with opposite momenta bind into Cooper pairs due to an attractive interaction mediated by phonons in the material. Although superconductivity naturally emerges at thermal equilibrium, it can also emerge out of equilibrium when the system parameters are abruptly changed[2–8]. The resulting out-of-equilibrium phases are predicted to occur in real materials and ultracold fermionic atoms, but not all have yet been directly observed. Here we realize an alternative way to generate the proposed dynamical phases using cavity quantum electrodynamics (QED). Our system encodes the presence or absence of a Cooper pair in a long-lived electronic transition in ^{88}Sr atoms coupled to an optical cavity and represents interactions between electrons as photon-mediated interactions through the cavity[9,10]. To fully explore the phase diagram, we manipulate the ratio between the single-particle dispersion and the interactions after a quench and perform real-time tracking of the subsequent dynamics of the superconducting order parameter using nondestructive measurements. We observe regimes in which the order parameter decays to zero (phase I)[3,4], assumes a non-equilibrium steady-state value (phase II)[2,3] or exhibits persistent oscillations (phase III)[2,3]. This opens up exciting prospects for quantum simulation, including the potential to engineer unconventional superconductors and to probe beyond mean-field effects like the spectral form factor[11,12], and for increasing the coherence time for quantum sensing.

Quantum simulation offers a path to understanding a broad range of phenomena, from high-temperature superconductivity and correlated quantum magnetism in condensed matter physics[13] to quarks and gluons in nuclei and matter under extreme conditions[14], as well as the black hole information paradox in gravitational physics[15]. A fascinating and promising case is the prethermal dynamical phases[16] predicted to emerge from quenches of superconductors and superfluids[2–8,17–22], systems that feature Cooper pairing of electrons or neutral fermions. There has been great progress in pump-probe experiments of superconductors that induce such fast quenches using terahertz technology, in which signs of phases I and II have been observed. However, the intense pulses couple nonlinearly to the Cooper pairs in the superconductor and complicate a clean observation of the dynamical phases[23–25]. For these reasons, the realization of fermionic superfluids in ultracold atomic gases[26] has generated great excitement[2–8]; however, to date observations have been limited to spectroscopic signatures rather than the full time dynamics[27]. In neither system has a systematic scan of the dynamical phase diagram been performed, and in fact, phase III has never been observed.

Here we take a step forward towards this challenge by using internal electronic states to encode effective Cooper pairs. At the heart of this implementation is the Anderson pseudo-spin mapping[28] by which the presence or absence of Cooper pairs in a momentum mode is encoded in a pseudo-spin-1/2 system. We simulate Anderson pseudo-spins using a long-lived electronic transition in ^{88}Sr with interactions between the spins mediated by a high-finesse optical cavity. As proposed in refs. 9,10, the scattering between Cooper pairs in condensed matter systems can be engineered in our system through the exchange of photons through the cavity (Fig. 1d). In this way, the dynamics of a collection of interacting spin-1/2 systems maps onto the low-energy physics of a superconductor or superfluid.

We probe all three dynamical phases (phases I, II and III) predicted to exist in Bardeen–Cooper–Schrieffer (BCS) superconductors by utilizing the high degree of control and flexibility in state initialization, interaction control and nondestructive measurements available when coupling long-lived atoms to an optical cavity. Behaviours intrinsic to phase I (normal phase) and phase II (finite steady-state superconductivity) have previously been observed in spin systems realized in optical cavities[29,30] and in two-level atoms interacting through collisions[31–34]. We build on this work by clarifying the connection between these dynamical phases from the BCS model and the physics of many-body gap protection in spin systems. Our results also provide a demonstration of phase III (a self-generated Floquet phase featuring persistent oscillations of the order parameter), which is predicted to dynamically

[1]JILA, NIST, and Department of Physics, University of Colorado, Boulder, CO, USA. [2]Center for Theory of Quantum Matter, University of Colorado, Boulder, CO, USA. [3]Max-Planck-Institut für Kernphysik, Heidelberg, Germany. [4]Homer L. Dodge Department of Physics and Astronomy, University of Oklahoma, Norman, OK, USA. [5]Center for Quantum Research and Technology, University of Oklahoma, Norman, OK, USA. [6]These authors contributed equally: Dylan J. Young, Anjun Chu. ✉e-mail: arey@jila.colorado.edu; jkt@jila.colorado.edu

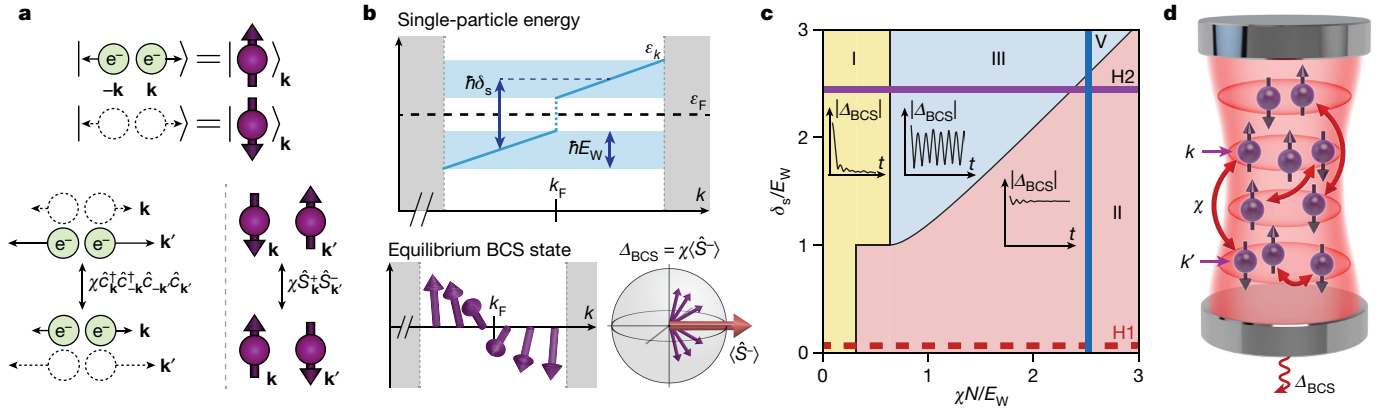

Fig. 1 | Engineering BCS dynamical phases. a, The Anderson pseudo-spin mapping encodes the presence and absence of a Cooper pair as the up and down states of a spin-1/2 system, respectively. Under this mapping, the attractive interaction $\chi\hat{c}^{\dagger}_{\mathbf{k}}\hat{c}^{\dagger}_{-\mathbf{k}}\hat{c}_{-\mathbf{k}'}\hat{c}_{\mathbf{k}'}$ between electrons is equivalent to an all-to-all exchange interaction $\chi\hat{S}^{+}_{\mathbf{k}}\hat{S}^{-}_{\mathbf{k}'}$ between pseudo-spins. **b**, Model parameters. The top plot shows the effective dispersion relation near the Fermi surface engineered in our system as a function of parameters δ_s and E_W, controlled using a.c. Stark shifts. The bottom plot visualizes the ground state of a BCS superconductor using Anderson pseudo-spins. Near the Fermi momentum, the pseudo-spins develop a phase-coherent superposition at a scale set by a non-zero BCS pairing gap Δ_{BCS}. This gap is self-consistently defined from the spin coherence as shown on the Bloch sphere. **c**, Dynamical phase diagram. The three dynamical phases can be realized by varying parameters χN, δ_s and E_W. Representative dynamics of the BCS order parameter $|\Delta_{BCS}|$ for each phase are shown as insets. We explore cut H1 (dashed line) in Fig. 2 using a single ensemble of atoms and cuts V and H2 (solid lines) in Figs. 3 and 4 using two separately controlled subensembles. **d**, Cavity QED implementation of the BCS interaction. Coupling many strontium atoms to a detuned optical cavity generates infinite-range spin-exchange interactions mediated by a virtual exchange of cavity photons. This interaction also causes a field proportional to Δ_{BCS} to leak out of the cavity, thus providing a real-time probe of the dynamics.

emerge in superconductors through quenches from weak to strong interactions[3,8]. In our system, we instead engineer this phase using flexible control of the single-particle dispersion[9,22], dynamically resembling the low-energy condition of a BCS superconductor. For all experiments, we perform real-time tracking of the superconducting order parameter, enabling a fast readout of the dynamics.

Experimental set-up and model system

To realize the dynamical phases of the BCS model, we laser cool an ensemble of $N = 10^5$–10^6 ^{88}Sr atoms and trap them inside a λ_L = 813 nm one-dimensional optical lattice supported by a high-finesse optical cavity. A spin-1/2 system is encoded in the electronic ground state $|\downarrow\rangle = |^1S_0, m_J = 0\rangle$ and a long-lived optical excited state $|\uparrow\rangle = |^3P_1, m_J = 0\rangle$, where m_J indicates the Zeeman sublevel of each state. Along this transition, we define spin operators $\hat{S}^{-}_k = |\downarrow\rangle_k\langle\uparrow|_k$ and $\hat{S}^{z}_k = (|\uparrow\rangle_k\langle\uparrow|_k - |\downarrow\rangle_k\langle\downarrow|_k)/2$ for single atoms with labels $k \in \{1, \ldots, N\}$, as well as the collective lowering operator $\hat{S}^{-} = \sum_k \hat{S}^{-}_k$ and raising operator $\hat{S}^{+} = (\hat{S}^{-})^{\dagger}$.

Assuming homogeneous atom–light coupling in the cavity and unitary dynamics, our system can be described by the Hamiltonian

$$\hat{H} = \hbar\chi\hat{S}^{+}\hat{S}^{-} + \sum_k \varepsilon_k\hat{S}^{z}_k. \quad (1)$$

The first term represents an infinite-range spin-exchange interaction described by a frequency scale χ (ref. 30), realized using the collective coupling between the atomic ensemble and a detuned optical cavity mode. Inhomogeneous atom–light coupling and dissipative processes (including, foremost, single-particle spontaneous decay) are present in the current implementation but do not largely change the qualitative behaviour of the targeted dynamical phases under our experimental conditions (Methods). Previously, we characterized this interaction[30] and studied the collective dynamics by applying an external drive[35]. In this work, we go beyond the fully collective manifold by engineering a spread in single-particle energies $\varepsilon_k = \hbar\omega_k$ using applied a.c. Stark shifts ω_k (refs. 36,37). These shifts form the second term in the Hamiltonian and compete with the spin-exchange interaction.

Equation (1) is the so-called Richardson–Gaudin spin model[38,39], which describes the low-energy physics of BCS superfluids and superconductors using the Anderson pseudo-spin mapping[28]. This mapping relates the presence (or absence) of a Cooper pair formed by a pair of electrons with momenta $\pm\mathbf{k}$ to a spin-up (or down) at momentum $\mathbf{k}$, as shown in Fig. 1a. Correspondingly, annihilating a Cooper pair maps to a spin-lowering operator by the relation $\hat{S}^{-}_{\mathbf{k}} := \hat{c}_{\mathbf{k}}\hat{c}_{-\mathbf{k}}$, where $\hat{c}_{\pm\mathbf{k}}$ are fermionic annihilation operators. Similarly, the spin operator $2\hat{S}^{z}_{\mathbf{k}} + 1 := \hat{c}^{\dagger}_{\mathbf{k}}\hat{c}_{\mathbf{k}} + \hat{c}^{\dagger}_{-\mathbf{k}}\hat{c}_{-\mathbf{k}}$ counts the number of electrons with momentum $\mathbf{k}$ or $-\mathbf{k}$. Our cavity system, therefore, manifestly implements a BCS superconductor if one identifies the label k of an atom in the cavity with the momentum $\mathbf{k}$ of the electrons in a Cooper pair. In this way, the first term in equation (1) is equivalent to the attractive interaction between electrons in the superconductor, and the second term can be associated with the kinetic energy or dispersion relation of the electrons. Note that the BCS model, described by equation (1), accounts only for the zero-momentum collective excitations present in conventional superfluids and superconductors[28].

The BCS order parameter in the Anderson mapping is defined by $\Delta_{BCS} = \chi\langle\sum_{\mathbf{k}}\hat{c}_{\mathbf{k}}\hat{c}_{-\mathbf{k}}\rangle = \chi\langle\hat{S}^{-}\rangle$, as depicted in Fig. 1b. In equilibrium, it plays the role of the BCS pairing gap, which energetically favours many-body states in which the electrons arrange in a coherent superposition between Cooper pairs and holes for states close to the Fermi energy. Away from equilibrium, Δ_{BCS} is also predicted to characterize the three dynamical phases (I, II and III) that arise after quenches in superconductors and superfluids[16]. Such dynamical phases represent distinct regimes of dynamical behaviour that arise after a sudden perturbation of a control parameter in a closed many-body system. They are described using a time-averaged or steady-state order parameter that demonstrates non-analytic behaviour at the boundary between phases. In particular, the BCS model is predicted to exhibit second-order dynamical phase transitions.

Phase I is characterized by a steady state with a vanishing order parameter $|\Delta_{BCS}(t)| \to 0$ at long times. Phase II exhibits a steady state with a constant non-zero order parameter $\Delta_\infty := \lim_{t\to\infty}|\Delta_{BCS}(t)| > 0$. Finally, phase III features oscillations in $|\Delta_{BCS}(t)|$ that persist to long times, realizing a Floquet superfluid despite not being periodically

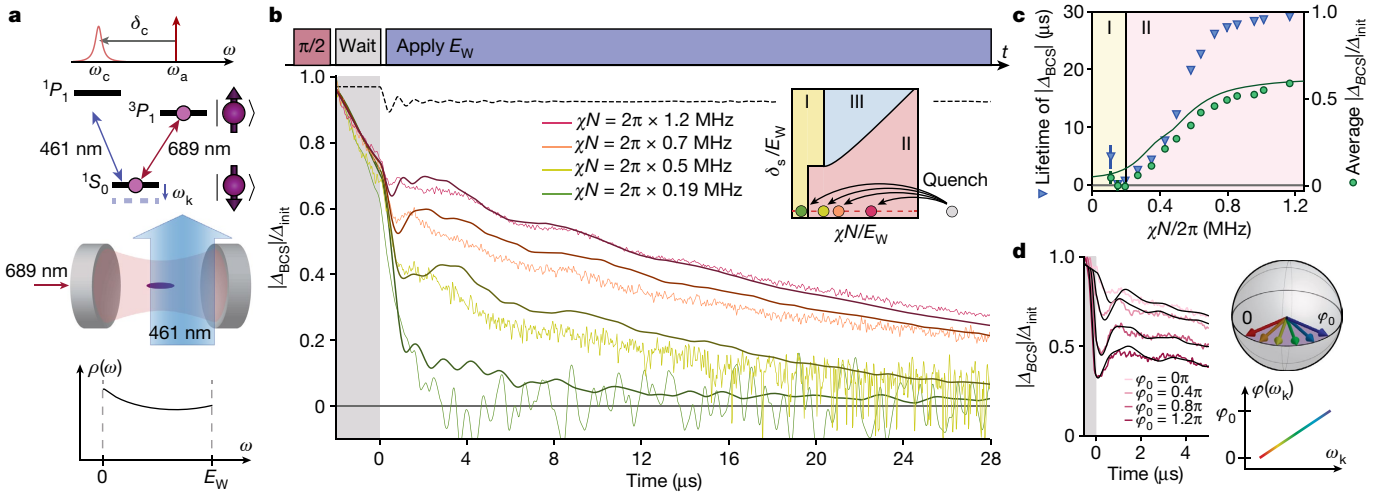

Fig. 2 | Phase I to phase II transition. a, Tuning the single-particle dispersion. We shine an off-resonant 461 nm beam onto the atoms from outside the cavity. This generates a distribution of a.c. Stark shifts representing a roughly uniform density of states $\rho(\omega)$ (bottom plot). **b**, Probing phase I and phase II. We apply a rapid π/2 pulse to prepare a highly coherent initial state, wait for 2 μs, quench to a variable $\chi N/E_W$ with $\delta_s = 0$ and then let the system evolve. The inset shows the explored parameter cut and identifies post-quench $\chi N/E_W$ values with coloured dots. The main plot shows experimental time traces of $|\Delta_{BCS}|$ (coloured curves) accompanied by numerical simulations (darker lines). Two curves are extended to demonstrate long-time coherence protection, with the $\chi N/2\pi$ = 0.19 MHz trace smoothed for clarity. For $\chi N/2\pi = 1.2$ MHz, we show an ideal simulation neglecting dissipation and motional effects (dashed line), which exhibits transient Higgs oscillations. Hints of these oscillations are present in experimental data with additional damping. **c**, Characterizing the phase transition. Blue triangles show the fitted coherence time of $|\Delta_{BCS}|$ from $t = 1$ to 30 μs. Green circles show the time-averaged $|\Delta_{BCS}|$ between $t = 3$ and 8 μs, with the dark green line representing numerical simulations. In all cases, we identify a phase transition at $\chi N/2\pi = 0.2$ MHz. Error bars in all plots represent the standard deviation of bootstrap resamplings on experimental shots (400–4,000 shots, $n = 100$ bootstrap resamplings). **d**, Varying the initial conditions. Before $t = 0$, we shine a high-intensity 461 nm beam within 300 ns, engineering an initial phase spread $\varphi(\omega_k) \in [0, \varphi_0]$ depicted on the Bloch sphere. The phase $\varphi(\omega_k)$ applied to atom k is proportional to the post-quench frequency shift ω_k. Traces represent different φ_0 and show enhanced oscillations with increasing φ_0.

driven[6–8,21]. The long-time behaviour of these dynamical phases admits a simpler description in terms of the Lax-reduced Hamiltonian, which is an effective Hamiltonian taking the same form as equation (1) but with rescaled parameters and a reduced number of spins[8,16]. Under this formulation, phases I, II and III emerge when the Lax-reduced Hamiltonian describes effective zero-spin, one-spin and two-spin systems, respectively.

Inspired by the Lax-reduced Hamiltonian and to explore all three dynamical phases, we engineer two subensembles of atoms with separate control over energy shifts within each subensemble. For practical convenience, we introduce an experimental control in the form of an overall frequency splitting δ_s between two subensembles and an effective frequency width E_W of each subensemble to engineer a tunable dispersion relation ε_k, as in Fig. 1b. Phases I and II can also be observed using a single ensemble of atoms, as shown in Fig. 2. Both experimental set-ups can, nonetheless, be described by a common phase diagram, as shown in Fig. 1c.

We initialize all the atoms in the $|\downarrow\rangle$ state and then apply a coherent π/2 pulse through the cavity in 100 ns such that $\Omega \gg \chi N$, where Ω is the pulse Rabi frequency and χN is the characteristic interaction strength for an ensemble of N atoms. This establishes a large BCS order parameter Δ_{BCS} on a timescale faster than any other relevant dynamics to mimic the ground state of a Hamiltonian with an infinite interaction strength χ. We then quench the system by rapidly turning on ε_k, which sets a finite ratio $\chi N/E_W$ and a variable δ_s/E_W, allowing us to explore the dynamical phase diagram shown in Fig. 1c.

We measure both the pre- and post-quench dynamics of $|\Delta_{BCS}|$ by monitoring light emitted by the atoms into the cavity as a function of time (Fig. 1d). This light arises from a superradiance process that is suppressed when the cavity resonance is detuned from the atomic transition frequency by much more than κ, the cavity power decay linewidth[40–42]. In this limit, the established cavity field adiabatically follows $\langle \hat{S}^- \rangle$, which is proportional to Δ_{BCS}. By measuring the leakage of light from the cavity in a heterodyne with a local oscillator, we, therefore, obtain a real-time probe of Δ_{BCS}. Importantly, at the chosen detuning, this probe is quasi-nondestructive, as only a small fraction of the atoms emit light over relevant timescales. In plots of $|\Delta_{BCS}|$ over time, we normalize traces to the initial gap size Δ_{init} measured right after the π/2 pulse.

Phase I to phase II

We probe the phase I to phase II transition by varying the ratio $\chi N/E_W$ between the interaction strength and the width of the single-particle energy distribution. As shown in Fig. 2a, we shine an off-resonant 461 nm beam onto a single atomic ensemble from the side of the cavity, which generates a distribution of a.c. Stark shifts with a spread E_W. Careful shaping of the 461 nm beam allows us to realize a roughly flat density of states (Methods), resulting in a set-up consistent with the $\delta_s = 0$ line in Fig. 1c (Supplementary Information). After the initial π/2 pulse, we wait for 2 μs to let transient dynamics settle and then turn on the 461 nm beam to quench on $E_W/2\pi = 0.83$ MHz from an initial value $E_W^{(0)}/2\pi \ll 0.1$MHz. The beam exhibits a rise time of roughly 50 ns, much faster than the relevant dynamics. To scan across the phase diagram in the inset of Fig. 2b, we vary the interaction strength χN between shots by changing the atom number N.

As shown in Fig. 2b,c, we observe two distinct dynamical behaviours corresponding to phases I and II, signalled by the decay rate of $|\Delta_{BCS}|$. For experiments with sufficiently small χN, such as $\chi N/2\pi = 0.19$ MHz, $|\Delta_{BCS}|$ decays with a 1/e coherence time of 0.9 ± 0.1 μs. This coherence time is consistent with single-particle dephasing of $\langle \hat{S}^- \rangle$ set by the energy spread $\hbar E_W$ and is nearly constant throughout this regime. We identify the fast decay of $|\Delta_{BCS}|$ as an experimental signature of phase I. For larger interaction strengths, we observe a rapid increase in the coherence time up to a maximum of 29 μs when $\chi N/2\pi = 1.2$ MHz; this constitutes an improvement by more than a factor of 30.

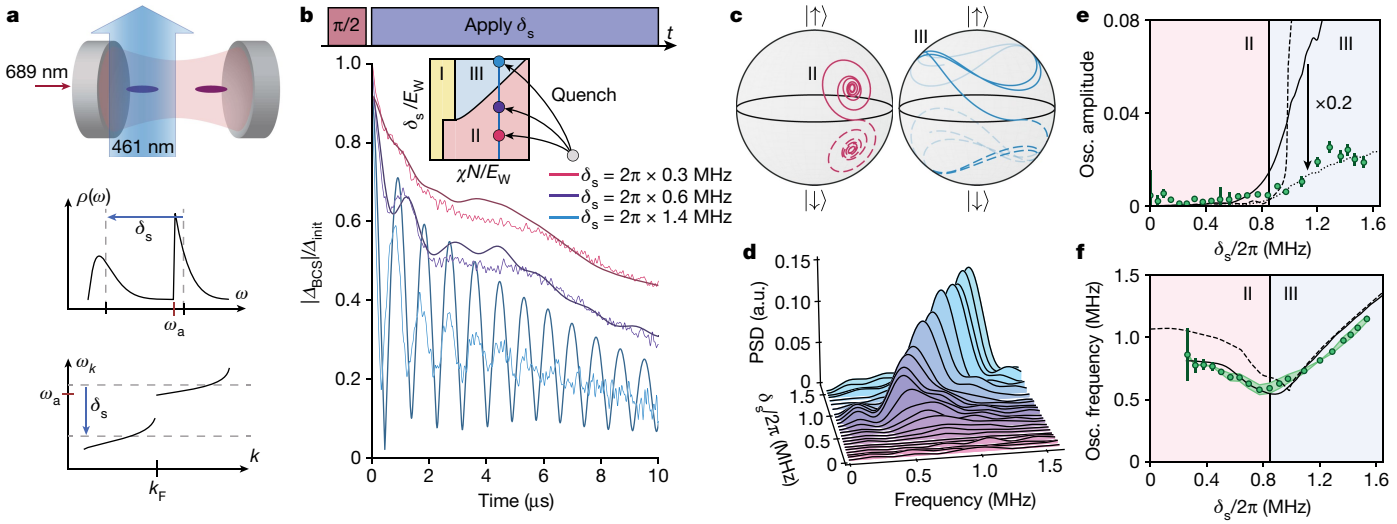

Fig. 3 | Phase II to phase III transition. a, Engineering a bimodal energy distribution. We prepare two atomic clouds with centres separated by 3 mm and shine an off-resonant 461 nm beam centred on one cloud. This generates a density of states $\rho(\omega)$ (middle plot), equivalent to a dispersion relation $\varepsilon_k = \hbar\omega_k$ (bottom plot). **b**, Probing phase II and phase III. We prepare the same initial state as in Fig. 2b with a π/2 pulse, quench to a finite δ_s/E_W and then let the system evolve. The inset shows the explored parameter cut and identifies post-quench δ_s/E_W values with coloured dots. As before, coloured traces represent experimental time traces of $|\Delta_{BCS}|$, and darker lines represent numerical simulations. **c**, Ideal simulations of mean-field trajectories for the two subensembles (solid and dashed curves) in phase II (magenta) and phase III (blue). The trajectories are projected onto the surface of the Bloch sphere for visual clarity. **d**, Fourier response of $|\Delta_{BCS}|^2$ for different δ_s, plotted as power spectral densities (PSDs) of the dynamics from $t = 0.5$ to 4.0 μs after subtracting slow-moving behaviour. **e**, Average oscillation amplitude between $t = 3$ and 8 μs. For the remaining plots, dashed lines represent ideal simulations (ignoring dissipation or motional effects), and solid dark lines correspond to full simulations. The additional dotted line represents numerical simulations rescaled by ×0.2, plotted to show similar trend behaviour between experimental data and simulations. We identify a phase transition around $\delta_s/2\pi = 0.85$ MHz. **f**, Oscillation frequency of $|\Delta_{BCS}|$, measured using power spectral densities calculated in **d**. We correct for systematics inferred from our data analysis and assume this correction has an uncertainty of 100%, as shown by the green band. The phase transition point observed in data in **e** and **f** agrees well with simulations. a.u., arbitrary units; Osc., oscillation.

We identify this extended coherence time regime as phase II. The residual decay of $|\Delta_{BCS}|$ in this regime can be attributed to intrinsic dissipative processes, including spontaneous emission, off-resonant superradiant emission and the scattering of 461 nm light[30,42], which set a maximum predicted coherence time of 29 μs (Methods). All experimental observations (coloured traces) are in good agreement with numerical simulations based on experimental conditions (dark lines; Methods).

Due to the separation of timescales in the decay of $|\Delta_{BCS}|$, we are able to determine the boundary between phase I and phase II in our experiment by calculating the average $|\Delta_{BCS}|$ in a time window from 3 to 8 μs as a function of χN (Fig. 2c). In this analysis, phase I features a vanishing average $|\Delta_{BCS}|$, whereas phase II has a non-zero $|\Delta_{BCS}|$ that increases with χN. The sharp rise of average $|\Delta_{BCS}|$ around $\chi N/2\pi = 0.2$ MHz indicates a dynamical phase transition, which agrees with the point predicted by numerical simulations. In a spin-model picture, the BCS pairing gap corresponds to the energy gap between collective angular momentum states, which exists due to the spin-exchange interaction $\chi\hat{S}^+\hat{S}^-$ (ref. 43). Phase II corresponds to the parameter region where such interactions are sufficiently strong to protect against single-particle dephasing. As a result, the observed transition directly relates to previous experiments exploring coherence protection in other systems[29–34].

In BCS superconductors, the excitation of a Higgs mode is predicted to occur in phase II. This mode can be characterized by a collective damped oscillation of the order parameter $|\Delta_{BCS}|$ with a characteristic frequency of $2\Delta_\infty$ (ref. 8). We observe hints of Higgs oscillations by comparing the experimental trace of $|\Delta_{BCS}|$ at $\chi N/2\pi = 1.2$ MHz (red curve in Fig. 2b) with the dissipation-free simulation (dashed line in Fig. 2b) and noticing that the first dip in the experimental trace coincides with the first cycle of Higgs oscillations (Methods). The size of this feature can be increased experimentally by engineering an initial phase spread $\varphi(\omega_k) \in [0, \varphi_0]$ between atoms that is correlated with the post-quench frequency shifts ω_k of the atoms, as shown in Fig. 2d. The initial state with a non-zero opening angle φ_0 shares qualitative features with the BCS ground state at finite χ up to a π/2 rotation on the Bloch sphere[9], in contrast to the initial state mimicking the BCS ground state with infinite χ in Fig. 2b.

Phase II to phase III

We probe the phase II to phase III transition using a vertical cut through the dynamical phase diagram. To realize this, we introduce an energy splitting $\hbar\delta_s$ between two individually addressable clouds of atoms along the cavity axis using a.c. Stark shifts from our 461 nm beam, as shown in Fig. 3a. In combination with a background energy spread $\hbar E_W$ associated with lattice shifts (Methods), this produces a bimodal density of states and a dispersion relation like the one proposed in Fig. 1b. As before, we begin the experiment with a highly coherent state and with $\delta_s = 0$. Then, we quench on a non-zero δ_s and let the system evolve. Between shots, we scan δ_s while fixing $\chi N/2\pi = 0.9$ MHz and $E_W/2\pi \approx 0.34$ MHz to explore the vertical cut.

The resulting dynamics show a marked change in the dynamical evolution of $|\Delta_{BCS}|$ over the scan, as shown in Fig. 3b, which we attribute to a transition between phase II and phase III dynamics. For small δ_s, we either see Higgs-like oscillations, which are damped after 3 μs (the trace where $\delta_s/2\pi = 0.6$ MHz), or, for very small splittings, no oscillations resolvable above the noise floor ($\delta_s/2\pi = 0.3$ MHz). We associate this regime with phase II, as it overlaps with the previously observed phase II dynamics in parameter space. For larger δ_s, the curves instead show large-amplitude oscillations that persist for more than 5 μs ($\delta_s/2\pi = 1.4$ MHz). We identify the long-lived oscillations in this parameter regime as an experimental signature of phase III.

Intuitively, we can understand the difference between the two phases by identifying the two subensembles of atoms with two Bloch vectors

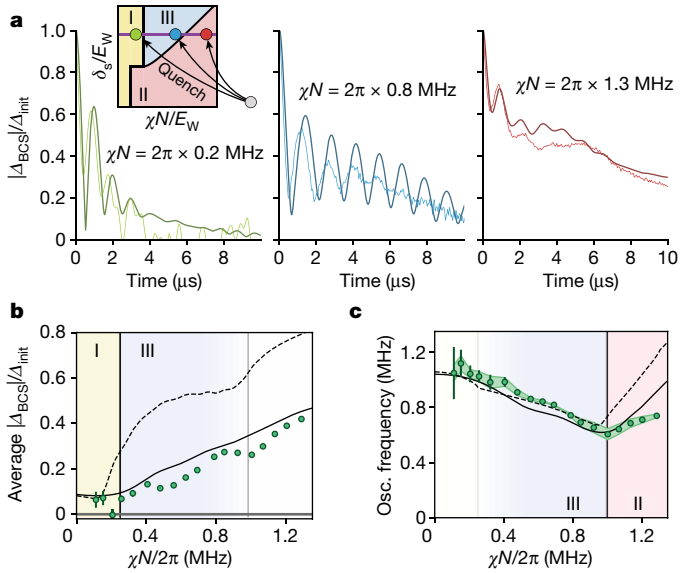

Fig. 4 | Scan across three dynamical phases. a, Probing phase I, II and III dynamics using time traces of $|\Delta_{BCS}|$. Quenches are performed in the same manner as in Fig. 3b, except between shots we hold post-quench values of δ_s fixed and vary χN instead. The inset shows the explored cut through the phase diagram and identifies final $\chi N/E_W$ values with green (phase I), blue (phase III) and red (phase II) dots. The $\chi N/2\pi = 0.2$ MHz trace is smoothed for clarity. **b**, Time average of $|\Delta_{BCS}|$ in a bin from $t = 3$ to 8 μs versus interaction strength. The experimental data shows signatures of a phase I to phase III transition at $\chi N/2\pi = 0.25$ MHz. **c**, Oscillation frequency of $|\Delta_{BCS}|$ versus interaction strength in a bin from $t = 0.5$ to 4.0 μs. Again, we correct for systematics inferred from our data analysis and assume this correction has an uncertainty of 100%, as shown by the green band. These data indicate a phase III to phase II transition at $\chi N/2\pi = 1.0$ MHz. Experimental data and transitions in both plots are consistent with numerical simulations.

(Fig. 3c). In phase II, a finite δ_s causes the Bloch vectors to precess in different directions, but the dominant scale χN locks them together to form the solid and dashed magenta orbits. In the presence of a finite E_W, the orbits decay, but the Bloch vectors maintain phase coherence. On the other hand, in phase III, δ_s is large enough that the two Bloch vectors accrue an unbounded relative phase, as in the blue orbits. The presence of interactions locks each subensemble separately against a finite E_W, leading to persistent oscillations. This effective beating of two large spins in a macroscopic array of spin-1/2 particles is truly an interaction-driven effect as the interactions are strong enough to lock the spins within each subensemble but not strong enough to lock both subensembles together. In our implementation of phase III, the bimodal distribution allows us to dynamically separate the Bloch vectors of the two subensembles, instead of starting with an already split distribution, like in weakly interacting BCS ground states featuring a sharp Fermi edge. Despite their qualitative differences, these two situations can be dynamically connected (Methods).

We can experimentally define a boundary between phase II and phase III using the separation of timescales observed for oscillations in $|\Delta_{BCS}|$. Figure 3e shows the average oscillation amplitude in a time window from $t = 3$ to 8 μs. In this analysis, we observe a sharp rise in the oscillation amplitude at $\delta_s/2\pi = 0.85$ MHz $\approx \chi N/2\pi$ as we increase δ_s, which we identify as a dynamical phase transition. The numerical simulations plotted in Fig. 3e agree fairly well with the data in capturing the trend and estimating the phase transition point. However, we see a discrepancy in the absolute size of the observed and predicted oscillation amplitudes. We attribute this to an extra dephasing mechanism (likely residual motional effects) in our system or other imperfections in the experimental sequence not captured by the theoretical model.

We verify the location of the phase II to phase III transition using the short-time oscillation frequency (from $t = 0.5$ to 4.0 μs) as an additional experimental signature. As can be seen in the Fourier responses in Fig. 3d and quantified in Fig. 3f, the oscillation frequency exhibits a dip versus δ_s at the previously identified phase boundary. This dip is present in roughly the same location in the experimental and theoretical results and is expected to coincide with the phase II to phase III transition (Supplementary Information).

Scan across three dynamical phases

Finally, we observe all three dynamical phases in a single cut through the parameter space, as shown in Fig. 4a. We run the same experimental sequence described in Fig. 3 but instead scan χN between shots with $\delta_s/2\pi = 1.1$ MHz and $E_W/2\pi = 0.46$ MHz fixed. This allows us to probe phase I, phase III and then phase II by increasing the atom number N. Using order parameters established in Figs. 2 and 3, we determine the boundaries between the three phases. As shown in Fig. 4b, the long-time average of $|\Delta_{BCS}|$ rises suddenly around $\chi N/2\pi = 0.25$ MHz in both data and simulations. This transition marks the boundary between phase I and phase III. Additionally, at $\chi N/2\pi = 1.0$ MHz, we observe a dip in the short-time oscillation frequency of $|\Delta_{BCS}|$ (Fig. 4c), which marks the transition between phase III and phase II. For this scan, we do not use the long-time oscillation amplitude as an order parameter due to the poor signal-to-noise ratio for smaller values of χN.

Conclusion

The demonstrated capability to emulate dynamical phases of superconductors in optical cavities opens exciting prospects for the field of quantum simulation. For example, it will be interesting to see if our cavity simulator can engineer and probe topological superfluid phases[7,44–49] or aid in understanding competing superconducting orders[50,51] in a single system. It may also be used to enable simulations of superfluidity in phenomena relevant to high energy physics[52,53].

Online content

Any methods, additional references, Nature Portfolio reporting summaries, source data, extended data, supplementary information, acknowledgements, peer review information; details of author contributions and competing interests; and statements of data and code availability are available at https://doi.org/10.1038/s41586-023-06911-x.

1. Bardeen, J., Cooper, L. N. & Schrieffer, J. R. Theory of superconductivity. *Phys. Rev.* **108**, 1175 (1957).
2. Yuzbashyan, E. A., Tsyplyatyev, O. & Altshuler, B. L. Relaxation and persistent oscillations of the order parameter in fermionic condensates. *Phys. Rev. Lett.* **96**, 097005 (2006).
3. Barankov, R. A. & Levitov, L. S. Synchronization in the BCS pairing dynamics as a critical phenomenon. *Phys. Rev. Lett.* **96**, 230403 (2006).
4. Yuzbashyan, E. A. & Dzero, M. Dynamical vanishing of the order parameter in a fermionic condensate. *Phys. Rev. Lett.* **96**, 230404 (2006).
5. Gurarie, V. & Radzihovsky, L. Resonantly paired fermionic superfluids. *Ann. Phys.* **322**, 2–119 (2007).
6. Gurarie, V. Nonequilibrium dynamics of weakly and strongly paired superconductors. *Phys. Rev. Lett.* **103**, 075301 (2009).
7. Foster, M. S., Dzero, M., Gurarie, V. & Yuzbashyan, E. A. Quantum quench in a $p+ip$ superfluid: winding numbers and topological states far from equilibrium. *Phys. Rev. B* **88**, 104511 (2013).
8. Yuzbashyan, E. A., Dzero, M., Gurarie, V. & Foster, M. S. Quantum quench phase diagrams of an s-wave BCS-BEC condensate. *Phys. Rev. A* **91**, 033628 (2015).
9. Lewis-Swan, R. J. et al. Cavity-QED quantum simulator of dynamical phases of a Bardeen–Cooper–Schrieffer superconductor. *Phys. Rev. Lett.* **126**, 173601 (2021).
10. Kelly, S. P., Thompson, J. K., Rey, A. M. & Marino, J. Resonant light enhances phase coherence in a cavity QED simulator of fermionic superfluidity. *Phys. Rev. Res.* **4**, L042032 (2022).
11. Stewart, G. R. Unconventional superconductivity. *Adv. Phys.* **66**, 75–196 (2017).
12. Sato, M. & Ando, Y. Topological superconductors: a review. *Rep. Prog. Phys.* **80**, 076501 (2017).
13. Zhou, X. et al. High-temperature superconductivity. *Nat. Rev. Phys.* **3**, 462–465 (2021).
14. Shuryak, E. Strongly coupled quark-gluon plasma in heavy ion collisions. *Rev. Mod. Phys.* **89**, 035001 (2017).

15. Harlow, D. Jerusalem lectures on black holes and quantum information. *Rev. Mod. Phys.* **88**, 015002 (2016).
16. Marino, J., Eckstein, M., Foster, M. & Rey, A.-M. Dynamical phase transitions in the collisionless pre-thermal states of isolated quantum systems: theory and experiments. *Rep. Prog. Phys.* **85**, 116001 (2022).
17. Volkov, A. F. & Kogan, S. M. Collisionless relaxation of the energy gap in superconductors. *J. Exp. Theor. Phys.* **38**, 1018 (1974). [Russian original—*Zh. Eksp. Teor. Fiz.* **65**, 2038 (1973)].
18. Yuzbashyan, E. A., Altshuler, B. L., Kuznetsov, V. B. & Enolskii, V. Z. Solution for the dynamics of the BCS and central spin problems. *J. Phys.: Math. Gen*. 38, 7831 (2005).
19. Barankov, R. A., Levitov, L. S. & Spivak, B. Z. Collective Rabi oscillations and solitons in a time-dependent BCS pairing problem. *Phys. Rev. Lett.* **93**, 160401 (2004).
20. Yuzbashyan, E. A. Normal and anomalous solitons in the theory of dynamical Cooper pairing. *Phys. Rev. B* **78**, 184507 (2008).
21. Foster, M. S., Gurarie, V., Dzero, M. & Yuzbashyan, E. A. Quench-induced Floquet topological *p*-wave superfluids. *Phys. Rev. Lett.* **113**, 076403 (2014).
22. Collado, H. P. O., Defenu, N. & Lorenzana, J. Engineering Higgs dynamics by spectral singularities. *Phys. Rev. Res.* **5**, 023011 (2023).
23. Mansart, B. et al. Coupling of a high-energy excitation to superconducting quasiparticles in a cuprate from coherent charge fluctuation spectroscopy. *Proc. Natl Acad. Sci. USA* **110**, 4539–4544 (2013).
24. Matsunaga, R. et al. Higgs amplitude mode in the BCS superconductors $Nb_{1-x}Ti_xN$ induced by terahertz pulse excitation. *Phys. Rev. Lett.* **111**, 057002 (2013).
25. Matsunaga, R. et al. Light-induced collective pseudospin precession resonating with Higgs mode in a superconductor. *Science* **345**, 1145–1149 (2014).
26. Randeria, M. & Taylor, E. BCS-BEC crossover and the unitary Fermi gas. *Annu. Rev. Condens. Matter Phys.* **5**, 209–232 (2014).
27. Behrle, A. et al. Higgs mode in a strongly interacting fermionic superfluid. *Nat. Phys.* **14**, 781–785 (2018).
28. Anderson, P. W. Random-phase approximation in the theory of superconductivity. *Phys. Rev.* **112**, 1900 (1958).
29. Davis, E. J. et al. Protecting spin coherence in a tunable Heisenberg model. *Phys. Rev. Lett.* **125**, 060402 (2020).
30. Norcia, M. A. et al. Cavity-mediated collective spin-exchange interactions in a strontium superradiant laser. *Science* **361**, 259–262 (2018).
31. Allred, J. C., Lyman, R. N., Kornack, T. W. & Romalis, M. V. High-sensitivity atomic magnetometer unaffected by spin-exchange relaxation. *Phys. Rev. Lett.* **89**, 130801 (2002).
32. Kleine, A., Kollath, C., McCulloch, I. P., Giamarchi, T. & Schollwoeck, U. Excitations in two-component Bose gases. *New J. Phys.* **10**, 045025 (2008).
33. Deutsch, C. et al. Spin self-rephasing and very long coherence times in a trapped atomic ensemble. *Phys. Rev. Lett.* **105**, 020401 (2010).
34. Smale, S. et al. Observation of a transition between dynamical phases in a quantum degenerate Fermi gas. *Sci. Adv.* **5**, eaax1568 (2019).
35. Muniz, J. A. et al. Exploring dynamical phase transitions with cold atoms in an optical cavity. *Nature* **580**, 602–607 (2020).
36. Baghdad, M. et al. Spectral engineering of cavity-protected polaritons in an atomic ensemble. *Nat. Phys.* **19**, 1104–1109 (2023).
37. Sauerwein, N. et al. Engineering random spin models with atoms in a high-finesse cavity. *Nat. Phys.* **19**, 1128–1134 (2023).
38. Richardson, R. & Sherman, N. Exact eigenstates of the pairing-force Hamiltonian. *Nucl. Phys.* **52**, 221–238 (1964).
39. Gaudin, M. Diagonalization of a class of spin Hamiltonians. *J. Phys.* **37**, 1087–1098 (1976).
40. Weiner, J. M., Cox, K. C., Bohnet, J. G., Chen, Z. & Thompson, J. K. Superradiant Raman laser magnetometer. *Appl. Phys. Lett.* **101**, 261107 (2012).
41. Bohnet, J. G., Chen, Z., Weiner, J. M., Cox, K. C. & Thompson, J. K. Active and passive sensing of collective atomic coherence in a superradiant laser. *Phys. Rev. A* **88**, 013826 (2013).
42. Norcia, M. A., Winchester, M. N., Cline, J. R. & Thompson, J. K. Superradiance on the millihertz linewidth strontium clock transition. *Sci. Adv.* **2**, e1601231 (2016).
43. Rey, A. M., Jiang, L., Fleischhauer, M., Demler, E. & Lukin, M. D. Many-body protected entanglement generation in interacting spin systems. *Phys. Rev. A* **77**, 052305 (2008).
44. Black-Schaffer, A. M. Edge properties and Majorana fermions in the proposed chiral *d*-wave superconducting state of doped graphene. *Phys. Rev. Lett.* **109**, 197001 (2012).
45. Nandkishore, R., Levitov, L. S. & Chubukov, A. V. Chiral superconductivity from repulsive interactions in doped graphene. *Nat. Phys.* **8**, 158–163 (2012).
46. Kiesel, M. L., Platt, C., Hanke, W., Abanin, D. A. & Thomale, R. Competing many-body instabilities and unconventional superconductivity in graphene. *Phys. Rev. B* **86**, 020507 (2012).
47. Kiesel, M. L., Platt, C., Hanke, W. & Thomale, R. Model evidence of an anisotropic chiral $d+id$-wave pairing state for the water-intercalated $Na_xCoO_2 \cdot yH_2O$ superconductor. *Phys. Rev. Lett.* **111**, 097001 (2013).
48. Fischer, M. H. et al. Chiral *d*-wave superconductivity in SrPtAs. *Phys. Rev. B* **89**, 020509 (2014).
49. Shankar, A. et al. Simulating dynamical phases of chiral $p+ip$ superconductors with a trapped ion magnet. *PRX Quantum* **3**, 040324 (2022).
50. Laughlin, R. Magnetic induction of $d_{x^2-y^2}+id_{xy}$ order in high-T_c superconductors. *Phys. Rev. Lett.* **80**, 5188 (1998).
51. Balatsky, A. V., Vekhter, I. & Zhu, J.-X. Impurity-induced states in conventional and unconventional superconductors. *Rev. Mod. Phys.* **78**, 373 (2006).
52. Schäfer, T. & Teaney, D. Nearly perfect fluidity: from cold atomic gases to hot quark gluon plasmas. *Rep. Prog. Phys.* **72**, 126001 (2009).
53. Pehlivan, Y., Balantekin, A., Kajino, T. & Yoshida, T. Invariants of collective neutrino oscillations. *Phys. Rev. D* **84**, 065008 (2011).

Methods

Experimental set-up for the phase I to phase II transition

To explore the phase diagram cut in Fig. 2, we first load 10^5–10^6 ^{88}Sr atoms from a magneto-optical trap into an 813 nm optical lattice supported by a high-finesse optical cavity, as in previous experiments[30,35,42,54]. The resulting atomic cloud has a temperature of roughly 15 μK, resulting in a Gaussian distribution transverse to the cavity axis with standard deviations $\sigma_y = \sigma_z = 16$ μm (coordinates defined in Extended Data Fig. 1a). Further, the cloud is extended over thousands of lattice sites to form a distribution along the cavity axis with a standard deviation $\sigma_x = 430$ μm. We measure an axial trapping frequency of $\omega_x/2\pi = 165$ kHz, which gives a Lamb–Dicke parameter of $\eta = 0.17$ for excitation with 689 nm light. At the measured temperature, $\eta^2(2\bar{n}+1) = 0.11 \ll 1$, thus placing the atoms in the Lamb–Dicke regime. We set a quantization axis along $\hat{y}$ with a 2.4 G magnetic field and tune the lattice polarization to a 'magic angle' relative to this axis such that the differential lattice shift between the ground ($|^1S_0\rangle$) and excited ($|^3P_1, m_J = 0\rangle$) states vanishes[35]. Using piezoelectric actuators, we stabilize the cavity length to set the closest TEM_{00} resonance to be 51 MHz red-detuned from the atomic transition.

After loading them into the lattice, we initialize the atoms with a $\hat{y}$-polarized drive through the cavity, which is nominally resonant with the atomic transition. Because the drive is far off-resonance from the cavity (which has linewidth $\kappa/2\pi = 153$ kHz at 689 nm), the induced Rabi frequency is somewhat suppressed. Nonetheless, we find that roughly 5 mW of power is needed before the cavity is sufficient to drive the atoms with a π/2 pulse in 100 ns. We allow the atoms to settle for 2 μs to distinguish the desired physics from any transient dynamics observed after state initialization, which we attribute to an undesired excitation of sideband transitions. We then shine a 461 nm beam from the side of the cavity along the $\hat{y}$ direction, detuned from the $|^1S_0\rangle \rightarrow |^1P_1\rangle$ transition by more than 10 GHz, to induce a.c. Stark shifts of the ground state. The beam has waists $(w_x, w_z) = (1{,}030\ \mu\mathrm{m}, 75\ \mu\mathrm{m})$ along the $\hat{x}$ and $\hat{z}$ directions at the plane of the atoms, and its centre is displaced from the centre of the atomic cloud by $x_0 = 580$ μm along the cavity axis. From these dimensions, we calculate an atomic density of states $\rho(\omega)$ as a function of the frequency shift which is roughly uniform between 0 and the maximum shift $\hbar E_W$. We estimate that for the power and detuning used in this cut, the 461 nm beam scatters off the atoms with an average rate of $R_{sc}/2\pi = 1.3$ kHz, roughly a factor of six smaller than $\gamma/2\pi = 7.5$ kHz, the spontaneous emission rate. Combined with the collective emission from the atoms as described in the 'Readout' section of Methods, these dissipation processes set a maximum predicted coherence time in the system of 29 μs.

Experimental set-up for the cuts through phase III

For the two cuts through phase III described in Figs. 3 and 4, we load the atoms into two clouds separated by 3 mm, as shown in Extended Data Fig. 1b. The left-hand cloud has an extent described by standard deviations $(\sigma_x, \sigma_z) = (200\ \mu\mathrm{m}, 16\ \mu\mathrm{m})$. The right-hand cloud has a similar extent along σ_z but is broader along the cavity axis. We tune the lattice polarization to point along $\hat{z}$, which breaks the magic angle condition and introduces a differential trap depth between the ground and excited states of 0.47 MHz for atoms experiencing the peak lattice intensity. Due to their finite temperature, the atoms experience a spread in lattice intensities, which leads to an inhomogeneous trap depth. We estimate the induced distribution of energy shifts by assuming the atoms occupy a two-dimensional Gaussian distribution radially with standard deviations $\sigma_y = \sigma_z = 16$ μm, compared to the lattice waists $w_y = w_z = 80$ μm. This produces a peaked distribution equivalent to the narrow peak in Fig. 3a.

In these experiments, we apply a π/2 pulse as before and then immediately shine a 461 nm beam centred on the left-hand ('bright') atomic cloud. Unlike for the previous cut, we do not wait for the transient dynamics to settle after state initialization, for simplicity. We do not see major differences between the observed and expected behaviour when omitting the wait period. The beam has waists $(w_x, w_z) = (1{,}700\ \mu\mathrm{m}, 80\ \mu\mathrm{m})$. We install a beam block just before the chamber to clip the beam tail, which otherwise would hit the right-hand ('dark') atomic cloud. The 3 mm separation between the clouds is sufficiently large to ensure that the beam does not significantly diffract around the beam block. The beam shifts the mean energy of the bright cloud away from that of the dark cloud, introducing a tunable δ_s. Although we nominally hold E_W fixed while scanning δ_s to explore the phase II to phase III transition, in reality the finite size of the blue beam introduces an additional contribution to E_W for the bright cloud. As δ_s increases, therefore, both the size and shape of the single-particle energy distribution change. We calculate E_W in a consistent manner by estimating the standard deviation of the bright cloud distribution and matching the result to a uniform distribution with the same standard deviation (Supplementary Information). In the main text, we report the value of E_W obtained at the phase transition point for the phase II to phase III transition. As we increase the 461 nm beam power, the atoms also scatter more blue photons. At the largest applied a.c. Stark shift, we estimate that the bright cloud experiences a scattering rate of $R_{sc}/2\pi = 3.4$ kHz, resulting in lower coherence times for traces with large δ_s. However, this excess decoherence does not bias our measurements of oscillation amplitude and frequency at times $t \leq 8$ μs.

Readout

After the initialization in all experiments, the atomic ensemble establishes a small electric field inside the cavity, which adiabatically follows $\langle \hat{S}^- \rangle$ (ref. 30). Assuming homogeneous atom–light coupling (see the next section for modifications due to inhomogeneous coupling), the complex amplitude of the electric field leaking out of the cavity is given by

$$\alpha_{\mathrm{out}}(t) = -\frac{g}{\delta_c}\sqrt{\kappa_m}\langle \hat{S}^-(t)\rangle, \tag{2}$$

where α_{out} has units of $\sqrt{\text{photons s}^{-1}}$. Here, $2g/2\pi = 10.6$ kHz is the single-photon Rabi frequency for an atom maximally coupled to the cavity, $\delta_c/2\pi = (\omega_c - \omega_a)/2\pi = -51$ MHz is the detuning between the cavity resonance frequency ω_c and the atomic transition frequency ω_a, and $\kappa_m/2\pi = 41$ kHz is the rate at which photons incident on the cavity mirror are transmitted. α_{out} is a form of dissipation in the system equivalent to superradiance in a detuned cavity limit. Over the region of parameter space explored in this work, we estimate that the dissipation rate never exceeds $\gamma_{SR}/2\pi = 2.3$ kHz. We measure the detuned superradiant light as it leaks out of the cavity using balanced heterodyne detection, which provide us with a real-time probe of $\langle \hat{S}^- \rangle \propto \Delta_{BCS}$. In plots of $|\Delta_{BCS}|$ in the main text, we calculate the square magnitude of this quantity and average over 400–1,600 shots of the experiment, taken within 2–10 min. We then subtract the background to remove the vacuum noise power from the heterodyne signal. Finally, we take a signed square root of the result to return an estimate of $|\Delta_{BCS}|$ which averages to 0 in the absence of a real signal. This explains why some traces dip below zero despite representing a nonnegative quantity.

Additionally, the cavity experiences a (dispersive) shift in its resonance frequency proportional to the number of atoms. We use this to measure the atom number by sending a pulsed probe tone through the cavity and measuring the frequency shift using the transmitted light. Since this light is spectrally resolved from the light emitted by the atoms, we are able to measure both signals independently on our heterodyne detector. The different optical frequencies involved in the heterodyne beat are compared in Extended Data Fig. 1c.

Dynamical phase diagram

The unitary dynamics of our system is modelled by an effective atom-only Hamiltonian, given by

$$\hat{H} = \hbar\chi \sum_{jk} \zeta_j \zeta_k \hat{S}_j^+ \hat{S}_k^- + \sum_k \varepsilon_k \hat{S}_k^z, \quad (3)$$

where $\hat{S}_k^{+,-}$ and $\hat{S}_k^{x,y,z}$ are the standard spin-1/2 operators on atom k. We define $\chi = -g^2\delta_c/(\delta_c^2 + \kappa^2/4)$, where g and δ_c are as defined in the previous section, and κ is the cavity linewidth. The spatial dependence of the interaction term is characterized by $\zeta_j = \cos(j\phi)$ with $\phi = \pi\lambda_L/\lambda_c$, which arises because the lattice wavelength $\lambda_L = 813$ nm is incommensurate with the cavity wavelength $\lambda_c = 689$ nm. In contrast to equation (1), equation (3) becomes non-integrable due to the inhomogeneity in the interaction term. Nevertheless, as shown in Extended Data Fig. 2, equation (3) leads to a similar dynamical phase diagram as equation (1) if we

1. Use a generalized superconducting order parameter $\Delta_{BCS} = \chi \sum_k \zeta_k \langle \hat{S}_k^- \rangle$.
2. Interpret the $\pi/2$ pulse as a pulse along the cavity axis under the Hamiltonian $\hat{H}_{drive} = \hbar\Omega \sum_k \zeta_k \hat{S}_k^y$ that generates the maximum possible $|\Delta_{BCS}|$, which occurs when $\Omega t = 0.586\pi$.
3. Replace the atomic number N by an effective atom number $N_{eff} = N/2$, such that χN_{eff} represents the averaged interaction strength of equation (3).

We can still measure the generalized order parameter Δ_{BCS} using the field leaking out of the cavity as in the previous section, since with inhomogeneous coupling the transmitted field takes the form $\alpha_{out}(t) = -\frac{g}{\delta_c}\sqrt{\kappa_m} \sum_k \zeta_k \langle \hat{S}_k^-(t) \rangle \propto \Delta_{BCS}$. The dynamical phase diagram in Extended Data Fig. 2 is numerically calculated based on unitary evolution under equation (3), with a single-particle dispersion $\varepsilon_k/\hbar$ sampled from a uniform distribution in the frequency ranges $[-\delta_s/2 - E_W/2, -\delta_s/2 + E_W/2]$ and $[\delta_s/2 - E_W/2, \delta_s/2 + E_W/2]$. There χN corresponds to the averaged interaction strength of equation (3). We identify the dynamical phases based on the long-time average of $|\Delta_{BCS}|$, given by

$$\mathrm{Avg}(|\Delta_{BCS}|) = \lim_{T\to\infty} \frac{1}{T} \int_0^T |\Delta_{BCS}(t)|\, \mathrm{d}t, \quad (4)$$

as well as the long-time oscillation amplitude of $|\Delta_{BCS}|$. Since the oscillations of $|\Delta_{BCS}|$ might deviate from a sinusoidal form, for theoretical simulations it is easier to use the standard deviation as a measure of the oscillation amplitude:

$$\mathrm{Std}(|\Delta_{BCS}|) = \left[\lim_{T\to\infty} \frac{1}{T} \int_0^T (|\Delta_{BCS}(t)| - \mathrm{Avg}(|\Delta_{BCS}|))^2\, \mathrm{d}t \right]^{1/2}. \quad (5)$$

When comparing with experimental data, we measure the oscillation amplitude using the Fourier spectrum because technical noise in the experiment contributes to the standard deviation of the time traces (Fig. 3d). The dynamical phases can be characterized in theoretical simulations by

- Phase I: $\mathrm{Avg}(|\Delta_{BCS}|) = 0$, $\mathrm{Std}(|\Delta_{BCS}|) = 0$.
- Phase II: $\mathrm{Avg}(|\Delta_{BCS}|) > 0$, $\mathrm{Std}(|\Delta_{BCS}|) = 0$.
- Phase III: $\mathrm{Avg}(|\Delta_{BCS}|) > 0$, $\mathrm{Std}(|\Delta_{BCS}|) > 0$.

The dynamical phase boundaries (white solid lines) in Extended Data Fig. 2 are analytically calculated using a Lax analysis applied to equation (1), like the one discussed in refs. 9,16, and take the following form (see Supplementary Information for a detailed derivation):

- Phase I to phase II:

$$\frac{\chi N}{E_W} = \frac{1}{\pi} \quad \text{with} \quad \frac{\delta_s}{E_W} \in [0, 1], \qquad \frac{\delta_s}{E_W} = 1 \quad \text{with} \quad \frac{\chi N}{E_W} \in \left[\frac{1}{\pi}, \frac{2}{\pi}\right]. \quad (6)$$

- Phase I to phase III:

$$\frac{\chi N}{E_W} = \frac{2}{\pi} \quad \text{with} \quad \frac{\delta_s}{E_W} > 1. \quad (7)$$

- Phase II to phase III:

$$\frac{\delta_s}{E_W} = \csc\left(\frac{E_W}{\chi N}\right) \quad \text{with} \quad \frac{\chi N}{E_W} > \frac{2}{\pi}. \quad (8)$$

The analytical results agree with the numerical simulations for equation (3). The only difference is that equation (1) predicts an extra dynamical phase transition marked by the white dashed line. The dynamical phase boundaries shown in Fig. 1c are constructed with the analytical formulas above.

Phase III dynamics with continuous single-particle dispersion

In this manuscript, we generate phase III using a bimodal single-particle dispersion, represented with idealized assumptions by Fig. 1b and with actual experimental conditions by Fig. 3a. Here we show that this experimentally convenient approach generates similar phase III dynamics to the one obtained for continuous dispersion but with different initial conditions.

This is done by the protocol shown in Extended Data Fig. 3a, which uses a bimodal distribution ($\delta_{s,init} > E_W$) just to generate a state with minimum $|\Delta_{BCS}|$. At this point, the system dispersion is restored to being continuous by setting $\delta_{s,final} = E_W$. This approach more closely resembles the phase III quench discussed in actual BCS superconductors, for which phase III is observed by quenching from a state with a weak BCS pairing gap $|\Delta_{BCS}|$ to one with a strong pairing gap[8]. Numerical simulations based on equation (3) show that nearly all choices of parameters that lead to phase III using a bimodal distribution also lead to phase III dynamics when quenching to a continuous distribution. The only exception is a small parameter regime close to the boundary between phase III and phase II (Extended Data Fig. 3b). Note that here we use definitions for Δ_{BCS}, the $\pi/2$ pulse, and χN that correspond to equation (3), as explained in the previous section.

Numerical simulations

The black dashed lines in Figs. 2, 3 and 4 are computed for a unitary evolution under equation (3) using a single-particle dispersion ε_k, sampled from the experimentally engineered distribution.

The black solid lines in the same figures are obtained by adding dissipative processes and axial motion to equation (3). The system dynamics is described by the following master equation for the density matrix $\hat{\rho}$:

$$\frac{\mathrm{d}\hat{\rho}}{\mathrm{d}t} = -\frac{\mathrm{i}}{\hbar}[\hat{H}, \hat{\rho}] + \mathcal{L}(\hat{L}_c)[\hat{\rho}] + \sum_k \mathcal{L}(\hat{L}_{s,k})[\hat{\rho}] + \sum_k \mathcal{L}(\hat{L}_{el,k})[\hat{\rho}]. \quad (9)$$

The Lindblad superoperator takes the form $\mathcal{L}(\hat{L})[\hat{\rho}] = \hat{L}\hat{\rho}\hat{L}^\dagger - \frac{1}{2}(\hat{L}^\dagger\hat{L}\hat{\rho} + \hat{\rho}\hat{L}^\dagger\hat{L})$. Superradiance through the cavity is described by the jump operator:

$$\hat{L}_c = \sqrt{\Gamma} \sum_k \zeta_k \hat{S}_k^-, \quad (10)$$

where $\Gamma = \chi\kappa/\delta_c$. Spontaneous emission from the atomic excited state is described by the jump operator:

$$\hat{L}_{s,k} = \sqrt{\gamma}\, \hat{S}_k^-, \quad (11)$$

where $\gamma/2\pi = 7.5$ kHz is the spontaneous emission rate out of $^3P_1$. Single-particle decoherence is described by the jump operator:

$$\hat{L}_{el,k} = \sqrt{2\gamma_{el}}\, \hat{S}_k^z, \quad (12)$$

where γ_{el} is a fitting parameter that takes into account free-space scattering from the a.c. Stark shift beam as well as other decoherence processes in the experiment (Supplementary Information). These are the dominant dissipative processes in our system.

The axial trapping frequency of the lattice is 165 kHz and is, therefore, smaller than the spin-exchange interaction rate χN for most of the experiments. As a consequence, in contrast to the idealized model in which atoms are assumed to be frozen, motional processes need to be accounted for, even though they are suppressed in the Lamb–Dicke regime. As shown in the Supplementary Information, axial motion can lead to a faster damping rate of $|\Delta_{BCS}|$ oscillations. The predicted dynamical phase boundaries are, nevertheless, unaffected by the axial motion.

All the numerical simulations are computed using the mean-field approximation, which replaces the operators $\hat{S}_k^{x,y,z}$ by their expectation values $\langle \hat{S}_k^{x,y,z} \rangle$ in the Heisenberg equation of motion. The mean-field treatment of the BCS model is predicted to be exact in the thermodynamic limit due to the infinite-range nature of the interactions[8]. The atom number for numerical simulation is set to 5,000 for the ideal conditions and 2,000 for actual experimental conditions. We rescale χ to match χN with experimental values.

Higgs-like behaviour in short-time phase II dynamics

When quenching into phase II, we observe highly damped oscillations of $|\Delta_{BCS}|$, reminiscent of the Higgs oscillations predicted to arise in this regime of the BCS model. Here, we analyse traces from Fig. 2d, in which we engineer a variable phase spread $\varphi(\omega_k) \in [0, \varphi_0]$ before quenching into phase II, to study this potential connection.

In the BCS model, Higgs oscillations can be characterized by their frequency, which should scale with the long-time BCS order parameter Δ_∞ as $\omega_{osc} = 2\Delta_\infty$ (ref. 8). We confirm this scaling in theory by measuring the oscillation frequency from $t = 0$ to $t = 5$ μs in idealized numerical simulations that ignore dissipation and motional effects (black dashed line in Extended Data Fig. 4a). For different values of the phase spread extent φ_0, the system reaches its steady state at a different long-time BCS gap Δ_∞. By parametrically plotting the oscillation frequency versus $2\Delta_\infty$ as a function of φ_0 in Extended Data Fig. 4c, we observe the expected scaling.

As discussed in the main text, the oscillations of $|\Delta_{BCS}|$ are consistently smaller and decay more quickly in the experimental data than in simulations. Nonetheless, we obtain a crude estimate of the experimental oscillation frequency by measuring a half period from the first trough and peak of $|\Delta_{BCS}(t)|$, as shown in Extended Data Fig. 4a. In Extended Data Fig. 4b, we compare the frequency in the experimental data to that of ideal simulations for different φ_0, which shows that the frequencies agree within the error bars. This suggests that the transient dynamics observed in $|\Delta_{BCS}|$ are related to the Higgs oscillations present in the theory.

Although the experimental oscillation frequency agrees with that from the simulations, the steady-state order parameter Δ_∞ is much smaller, as can be seen in Extended Data Fig. 4a. As a result, the measured frequencies scale linearly with Δ_∞ but with a different prefactor. In Extended Data Fig. 4c, we fit a linear relation $\omega_{osc} = (1.7^{+0.7}_{-0.4}) \times 2\Delta_\infty$ to the data. The uncertainty bounds for the slope are calculated by assuming that the errors in ω_{osc} are perfectly correlated. Most of the reduction in Δ_∞ can be captured in theory by considering dissipation and motional effects (solid black trace). We see an additional small difference in $|\Delta_{BCS}|$ between full numerical simulations and experimental data, which we attribute to drifts in experimental alignments and calibration factors over time. This difference is not apparent in Fig. 2d because we plot $|\Delta_{BCS}|$ in normalized units.

Data availability

The datasets generated for this study are available in a Dryad repository with the identifier https://doi.org/10.5061/dryad.7h44j100j (ref. 55).

54. Norcia, M. A. et al. Frequency measurements of superradiance from the strontium clock transition. *Phys. Rev. X* **8**, 021036 (2018).
55. Young, D. J. et al. Data for: observing dynamical phases of BCS superconductors in a cavity QED simulator. *Dryad* https://doi.org/10.5061/dryad.7h44j100j (2023).

Acknowledgements This material is based upon work supported by the US Department of Energy, Office of Science, National Quantum Information Science Research Centers, Quantum Systems Accelerator. We acknowledge additional funding support from the National Science Foundation under Grant Nos. 2317149 (Physics Frontier Center) and OMA-2016244 (Quantum Leap Challenge Institutes), the National Institute of Standards and Technology, the Army Research Office of the Defense Advanced Research Projects Agency (Grant Nos. W911NF-19-1-0210 and W911NF-16-1-0576) and the Air Force Office of Scientific Research (Grant Nos. FA9550-18-1-0319 and FA9550-19-1-0275). We acknowledge helpful discussions with E. Yuzbashyan, V. Gurarie and A. Kaufman.

Author contributions D.J.Y., E.Y.S., Z.N., V.M.S. and J.K.T. collected and analysed the experimental data. A.C., D.B., D.W., R.J.L.-S. and A.M.R. developed the theoretical model. All authors discussed the results and contributed to the preparation of the manuscript.

Competing interests The authors declare no competing interests.

Additional information

Supplementary information The online version contains supplementary material available at https://doi.org/10.1038/s41586-023-06911-x.

Correspondence and requests for materials should be addressed to Ana Maria Rey or James K. Thompson.

Peer review information *Nature* thanks José Lorenzana, Emil Yuzbashyan and the other, anonymous, reviewer(s) for their contribution to the peer review of this work.

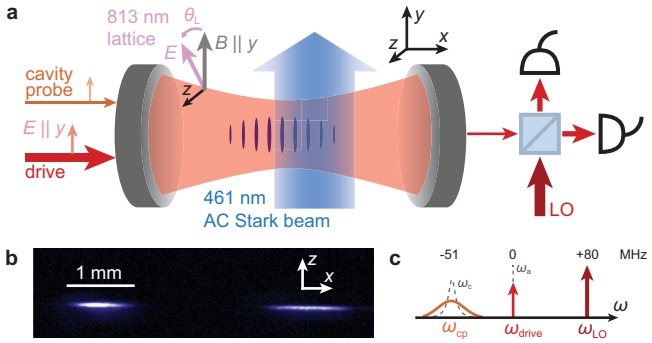

Extended Data Fig. 1 | Experimental configuration. a, Detailed diagram of the cavity and all relevant beams. A magnetic field along $\hat{y}$ sets the quantization axis. The 813 nm optical lattice supported by the cavity has a tunable linear polarization. We drive a $\pi/2$ pulse with a beam polarized along $\hat{y}$ through the cavity, and during the experiment we probe the cavity resonance frequency using a second $\hat{y}$-polarized beam to measure atom number. A 461 nm beam far-detuned from the $|^1S_0\rangle \rightarrow |^1P_1\rangle$ transition shines on the atoms from the side of the cavity, inducing a.c. Stark shifts. We probe signals transmitted through the cavity using a balanced heterodyne detector. **b**, Fluorescence image of the two atomic clouds used when scanning through phase III in Figs. 3 and 4. **c**, Frequency landscape of 689 nm beams. The atomic drive frequency ω_{drive} is resonant with the atomic transition. The cavity probe frequency ω_{cp} is nominally centred with the cavity resonance frequency, 51 MHz red-detuned from the atomic transition. The local oscillator used in heterodyne detection has frequency ω_{LO} and is 80 MHz blue-detuned from the atomic transition.

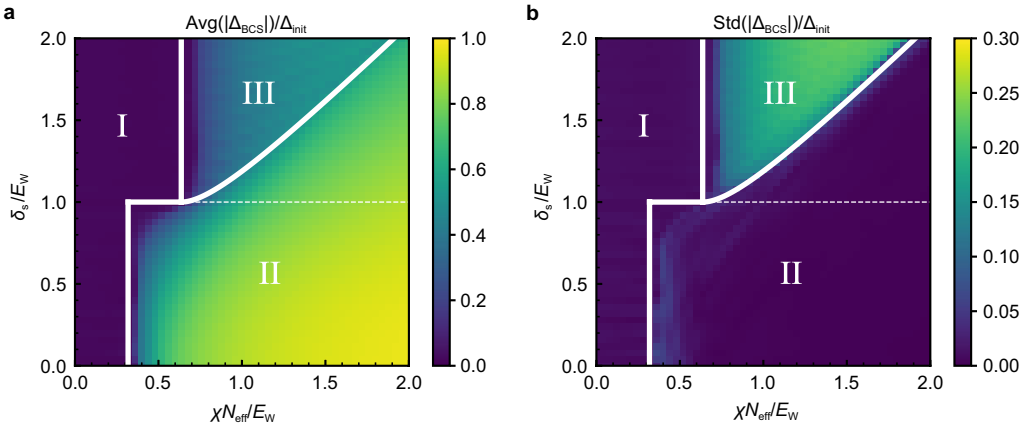

Extended Data Fig. 2 | Numerical simulation of the dynamical phase diagram based on equation (3). We identify the dynamical phases based on the long-time average (**a**) and the long-time standard deviation (**b**) of $|\Delta_{BCS}(t)|$, normalized by its initial value $\Delta_{init} \equiv |\Delta_{BCS}(0)|$. The white solid lines mark the corresponding dynamical phase boundaries, analytically derived from equation (1), which agree with the numerical results based on equation (3). The white dashed lines mark an extra dynamical phase transition that only exists for equation (1).

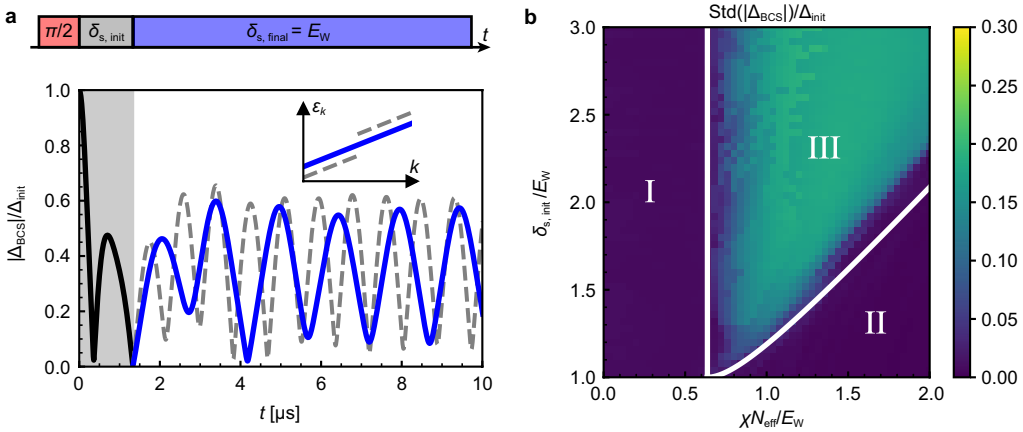

Extended Data Fig. 3 | Alternative approach for phase III. a, Simulation of an alternative experimental sequence. As described by the timing sequence at the top, we simulate an experiment that prepares the initial state using a π/2 pulse, lets the system evolve under a bimodal distribution of single-particle energy (see the inset) until $|\Delta_{BCS}|$ reaches its minimum value and then quenches the system back to a continuous distribution of single-particle energies (inset). The theoretically predicted time trace of $|\Delta_{BCS}|$ with $\chi N/E_W = 1.0$ and $\delta_{s,init}/E_W = 1.6$ is shown at the bottom. The blue (grey dashed) line shows phase III dynamics under a continuous (bimodal) distribution. **b**, Long-time standard deviation of $|\Delta_{BCS}(t)|$ after quenching to the continuous distribution shown in **a**. The white lines are dynamical phase boundaries for bimodal distributions (see Extended Data Fig. 2). Nearly all choices of parameters for phase III using bimodal distributions can lead to phase III behaviour after quenching to the continuous distribution.

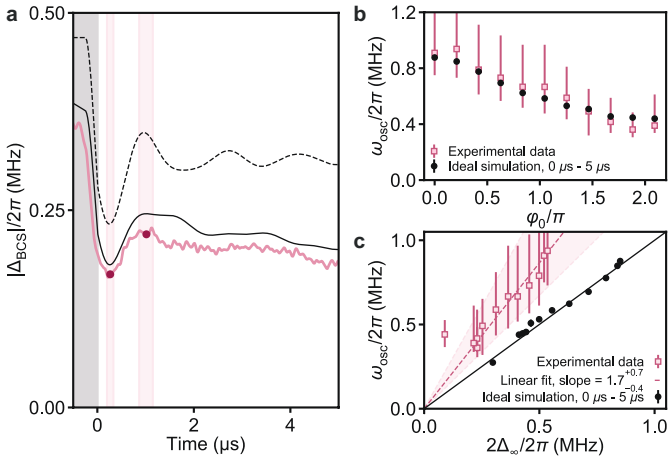

Extended Data Fig. 4 | Collective scaling in damped phase II oscillations. **a**, Time dynamics of $|\Delta_{BCS}|$ measured after engineering an initial phase spread over $[0, \varphi_0]$ where $\varphi_0 = 0.8\pi$ as in Fig. 2d, plotted in absolute frequency units (pink trace). The solid black curve represents a numerical simulation of the full system, whereas the dashed curve represents an ideal simulation neglecting dissipation and motional effects. We obtain a crude estimate of oscillation frequency in the experimental data by fitting a trough and peak to smoothed data (after subtracting slow-moving behaviour) within the first couple μs (magenta points), using these points to infer a half period of oscillation, and with uncertainties determined using a 90% amplitude threshold (pink bands). **b**, Comparing oscillation frequency estimates of experimental data (pink squares) with those of ideal simulations (black dots) for different φ_0. Theory oscillation frequencies are calculated using a Fourier transform from $t = 0$ μs to $t = 5$ μs. Error bars for experimental data are set by the minimum and maximum frequencies implied by uncertainties in the half period shown in **a**. The two frequency estimates agree within error bars. **c**, Collective scaling of oscillation frequency. For each φ_0 measured in the experiment, we plot the oscillation frequency against the long-time BCS gap Δ_∞, calculated at $t = 18$ μs for ideal simulations and at $t = 3$ μs for experimental data. The solid black line is defined by $\omega_{osc} = 2\Delta_\infty$, demonstrating the expected scaling for Higgs oscillations. The dashed pink line represents a linear fit to the experimental data. The pink band shows the uncertainty in the slope assuming correlated error in ω_{osc}, such that its bounds are defined by linear fits to the data assuming maximum and minimum values for ω_{osc} as defined by the error bars.